Automotive Science and Engineering, Vol. 14, No. 3, (2024), 4472-4478

Iran University of Science and Technology

Automotive Science and Engineering

Journal Homepage: ase.just.ac.ir

ISSN: 2008-9899

The enhancement of the specific capacity of $Ti_3C_2T_x$-based Li-O_2 battery by adding super-p

Reza Azadvari [1], Somayeh Mohammadi [2]*, Zeinab Sanaee [3], Khadijeh Hooshyari [4]

[1]Ph.D. graduate student, Energy Storage Laboratory, School of Electrical and Computer Engineering, College of Engineering, University of Tehran, Tehran, Iran.

[2,*]Assistant Professor, School of Engineering Science, College of Engineering, University of Tehran, Tehran, Iran.

[3]Associate Professor, Energy Storage Laboratory, School of Electrical and Computer Engineering, College of Engineering, University of Tehran, Tehran, Iran.

[4] Assistant Professor, Faculty of Chemistry, Department of Applied Chemistry, Urmia University, Urmia, Iran

ARTICLE INFO

Article history:

Received : 2 May 2024

Accepted: 3 Aug 2024

Published: 4 Sep 2024

Keywords:

$Ti_3C_2T_x$

MXene

Li-O_2 battery

super p

A B S T R A C T

This work investigated the effect of super p on the specific capacity of MXene-based rechargeable Li-O_2battery. It was observed that by changing the ratio of super P from 10% to 30%, the specific discharge capacity of the lithium-oxygen battery has been enhanced from 396 $mAhg^{-1}$ to 1116 $mAhg^{-1}$ in the 1st cycle at the current density of 100 mAg^{-1}. To analyze the structure of synthesized MXene, techniques such as scanning electron microscopy (SEM), X-ray diffraction (XRD), Raman spectroscopy, and Fourier transform infrared (FTIR) spectroscopy were employed. The electrochemical properties of the fabricated electrodes were assessed using cyclic voltammetry (CV) and electrochemical impedance spectroscopy (EIS). Based on the analysis, the synergistic effect between MXene and Super P results in a higher capacity for the fabricated cell.

1. Introduction

The first experimental observations of the lithium-oxygen battery were conducted by Abraham and colleagues in 1996, and it has been under investigation since 1974[1, 2]. In recent years, the impressive theoretical energy density of lithium-oxygen batteries has positioned them as a leading candidate for use in portable electronic devices and electric vehicles compared to lithium-ion batteries[3-6]. In these batteries, the anode electrode is made of pure lithium metal, while the cathode electrode is comprised of carbon-based materials and metal oxides, particularly in the form of two-dimensional structures [7, 8]. Additionally, aprotic electrolytes like LiTFSI/TEGDME are commonly used as the electrolyte and glass fiber or Celgard are used as the separator [9, 10].

At the cathode electrode, two very important reactions, namely the oxygen reduction reaction (ORR) in the discharge process and the oxygen evolution reaction (OER) in the charge process, lead to the formation and decomposition of lithium peroxide (Li_2O_2), respectively[1, 7, 11-13].

A significant challenge in these batteries arises from the sluggish kinetics of the ORR and OER, which leads to charge and discharge overpotential. Consequently, this results in low round-trip efficiency, inadequate rate capability, and limited cycle stability. These issues have hindered the

*Corresponding Author
Email Address: so.mohammadi@ut.ac.ir
http://doi.org/10.22068/ase.2024.674

current commercialization of Li-O_2 batteries [3, 5, 11].

Over the last decade, researchers have shown considerable interest in two-dimensional MXene nanomaterials, particularly Titanium carbide ($Ti_3C_2T_x$), for energy storage devices such as supercapacitors, lithium-ion batteries, and more recently, lithium-oxygen batteries, owing to their distinctive chemical and electrical properties [7, 14-16]. MXene nanomaterials have a three-layer structure with the formula $M_{n+1}X_nT_x$. In this formula, M represents a transition metal, X stands for either carbon or nitrogen, and T_x denotes surface functional groups such as –F, –OH, and –O [4, 17-20].

One common approach to creating $Ti_3C_2T_x$ nano-layers involves etching away the aluminum (Al) layers from Ti_3AlC_2 using lithium-ion-containing solutions such as HF or LiF/HCl [21-25].

Despite the unique properties of $Ti_3C_2T_x$ MXene, like most other 2D materials, the stacking of layers deteriorates its ion storage capability. Additionally, its electrical conductivity decreases due to surface and edge defects. To overcome these problems, various additives including carbon-based nano-materials, organic molecules, and metal ion or oxide nano-particles are introduced between the MXene layers [18, 23, 26].

In recent years, there have been several reports of using $Ti_3C_2T_x$ in Li-O_2 battery. For example, in 2023, Xingzi Zheng et al. investigated a $Ti_3C_2T_x$ MXene-based Li-O_2 battery and improved its battery capacity and cycle life[3].

In another report, Sanghee Nam et al. designed a lithium-oxygen battery with $Ti_3C_2T_x$ MXene and achieved high capacity by controlling ORR and OER in the cathode[27].

Generally, if the slurry method is used for the fabrication of electrodes in Li-ion batteries, carbon nanomaterials such as carbon black, Ketjen Black, and Super P are commonly used in various amounts to enhance the overall conductivity of the electrode. These materials are also sometimes used as active materials in the cathode of the Li-O_2 batteries[7, 28].

For example, Zheng et al. used Ketjen Black both as a conductive material and an active material with a 45% and 90% mass ratio, respectively [11]. In another research, Zhao et al. added Super P as both conductive material and active material with 40 % and 80% mass ratio, respectively [28].
Although it seems that various amounts of carbon nanomaterials can significantly improve the parameters of the Li-O_2 battery, this aspect has unfortunately been overlooked until now.

This research focused on examining the effect of Super P on the ion storage capability of $Ti_3C_2T_x$ for use as a cathode in a lithium-oxygen rechargeable battery. By changing the ratio of Super P from 10% to 30%, the specific discharge capacity of the Li-O_2 battery increased to 180% in the first cycle at a current density of 100 mA g^{-1}.

2. Methods and Materials

2.1. Formulation of Ti_3AlC_2 MAX phase

To synthesize Ti_3AlC_2, a mixture of graphite (grain size lower than 45 micron), Titanium (grain size lower than 20 microns), and Aluminum (grain size lower than 20 microns) powders was used with a 1.9:3:1.4 molar ratio. Next, the powders were ball-milled at a rate of 400 rpm, with a 10:1 pellet-to-powder ratio in an argon atmosphere for 18 hours, with 10-minute breaks each hour. After ball milling, the powder is poured into a graphite mold in a cylindrical shape with an internal diameter of 30 mm and placed in the Spark-plasma sintering (SPS) machine.

The final phase of Ti_3AlC_2 MAX is produced by applying an electric current and uniaxial pressure of 35 MPa simultaneously for 15 minutes at 1100°C, raising the temperature to 1100°C at a rate of 50-80°C per minute.

2.2. Formulation of $Ti_3C_2T_x$ MXene

To achieve MXene nano-sheets, the Al layers were selectively etched of the Ti_3AlC_2 MAX-phase using an HF solution (40 wt %). The MAX- phase was dispersed and stirred in the acid solution at 40 °C for 30 hours. After the etching process, to attain a neutral pH, MXene powders were rinsed multiple times with deionized water and then kept under vacuum at 80°C for 24 hours to ensure complete drying.

2.3. Analysis of materials

To characterize the synthesized materials, Field Emission Scanning Electron Microscopy (FE-SEM, S-4160, Hitachi, Japan) at 20 kV, X-ray Diffraction (XRD) using the X'Pert PRO MPD system (Panalytical, CuKα radiation, λ = 0.15406 nm), Raman spectroscopy was conducted using Apus + Raman microscope (DPSS Nd: YAG (cw)) with a 532-nm wavelength laser beam, and Fourier Transform Infrared Spectrometry (TENSOR II FTIR Routine Spectrometer from Bruker Optics) were used.

2.4. Battery Assembly

[DOI: 10.22068/ase.2024.674]

.

Two different Li-O_2 battery cathodes were fabricated by combining $Ti_3C_2T_x$, super P, and polyvinylidene fluoride (PVDF) as a binder in N-methyl-2-pyrrolidinone (NMP) with varying ratios of weight of 80: 10: 10 and 60: 30:10, respectively. Afterward, the uniform slurry was evenly spread on carbon paper (GP-H-030, Toray) (which is used as a gas diffusion layer) and dried overnight at 80°C under a vacuum oven. The loading mass of the total active material was around 0.4 mg. Based on the mass of the active material, the specific capacity and current density of the electrodes are determined. The components of the Li-oxygen battery include a lithium foil anode, a glass fiber separator (Whatman, GF/D), a 1 M LiTFSI/TEGDME electrolyte (MerckScientific, 99.95%), and a cathode. These components are assembled in an argon-filled glove box (manufactured by Armaghan Diyar Daryush Company), maintaining oxygen and water levels below 0.5 ppm. All components of the battery were assembled into a CR2032 coin cell, which features a porous can on the cathode side. As depicted in Figure 1, after being placed inside the lithium-oxygen battery setup, the cell underwent testing using the NEWARE multi-channel battery tester system within a voltage range of 2 to 4.5 volts.

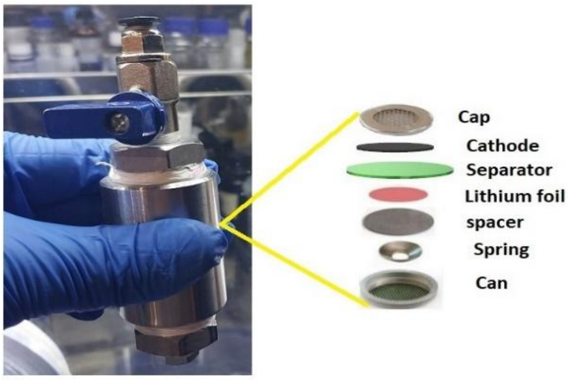

Figure 1. Lithium-oxygen battery setup

3. Findings and Analysis

3.1. Material analysis

In Figure 2(a) the SEM image of prepared Ti_3AlC_2 is shown. MAX-phase micro-zones can be easily seen in this figure. The SEM images of the 2D structure of pristine $Ti_3C_2T_x$ and 30% Super-P added $Ti_3C_2T_x$ are presented in Figures 2(b)& (c), respectively. The red arrows in Figure 2-(c) point to some of the Super P nano-grains that are distributed between the MXene nano-sheets.

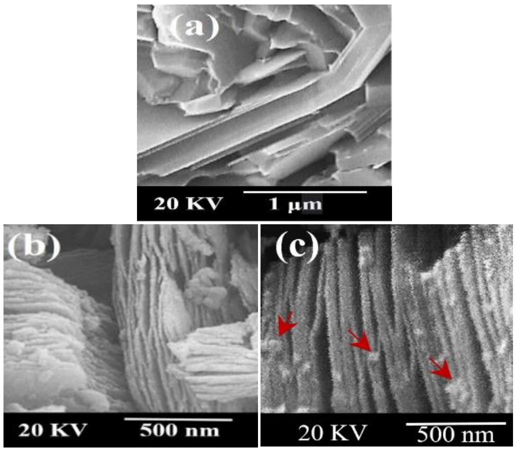

Figure 2. SEM images of (a) Ti_3AlC_2 MAX-phase, (b) $Ti_3C_2T_x$ nano-sheets, (c) Super P/$Ti_3C_2T_x$ nano-composite.

To further investigate the structure of the synthesized materials and confirm the formation of MAX-phase and MXene, their XRD patterns are presented in Figure 3.

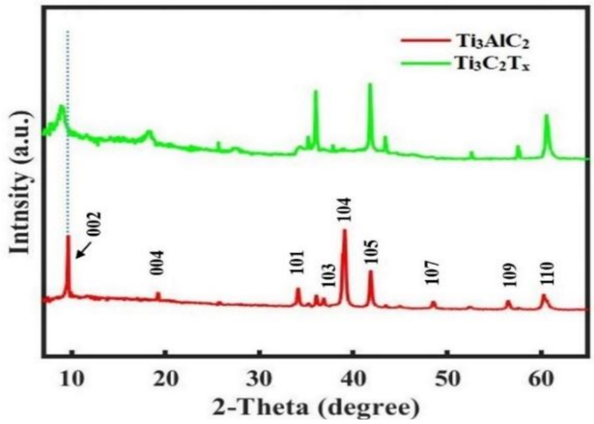

Figure 3. XRD patterns of Ti_3AlC_2 MAX-phase and $Ti_3C_2T_x$ nanosheets.

In the XRD pattern of Ti_3AlC_2 (red curve), the characteristic peaks of Ti_3AlC_2 related to the (002) at 9.66°, (004) at 19.21°, (101) at 34.13°, (103) at 36.08°, (104) at 39.07°, (105) at 41.83°, (107) at 48.51°, (109) at 56.49°, and (110) at 60.29° crystal planes are present. Moreover, in the XRD pattern of the $Ti_3C_2T_x$ (green curve), the important characteristic peaks of $Ti_3C_2T_x$ including 9.06° referred to the (002) crystal plane, and 18.35° related to the (004) crystal plane are present.

The peaks corresponding to the (002) plane of the MXene sample show a leftward shift compared to the MAX-phase one. This shift indicates an increase in interlayer spacing arising from the removal of Al atoms. Figure 4 presents FTIR spectroscopy to further explore the structural properties of the synthesized MXene. In this figure, the wide peak near 3500 cm^{-1} and the peak at 1385 cm^{-1} are associated with –OH groups [29-32]. In addition, the peaks at 531 and 465 correspond to Ti-O bonding, and the peak at 610 corresponds to Ti-C bonding [33-35]. These peaks can confirm the presence of $Ti_3C_2T_x$ structure with the -OH and -O functional groups.

The Raman spectrum of pristine $Ti_3C_2T_x$ is presented in Figure 4(b). In this spectrum, the G-band of $Ti_3C_2T_x$ is located at 1574 cm^{-1}, which can be ascribed to the in-plane stretching vibration of hybridized sp^2 carbon atoms [17]. The D band is present at 1379 cm^{-1}, illustrating the presence of defects in the carbon lattice.

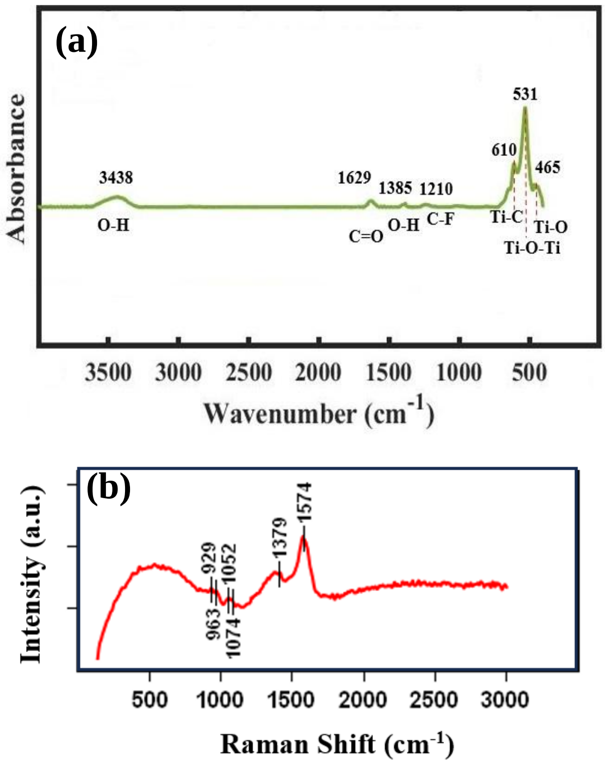

Figure 4. (a) FTIR spectra and (b) Raman spectra of $Ti_3C_2T_x$ MXene nano-layers.

3.2. Electrochemical measurements

To explore the electrochemical performance of the fabricated Li-O_2 batteries, their Galvanostatic discharge-charge profiles at a current density of 100 mAg^{-1} are displayed in Figure 5-(a) & (b). As presented in Figure 5-(a), the Li-O_2 battery with a low Super P/$Ti_3C_2T_x$ ratio (10:80) in its cathode provided a discharge-specific capacity of 396 $mAhg^{-1}$ in the 1st cycle and 298 $mAhg^{-1}$ and 196 $mAhg^{-1}$, in the 2nd and 3rd cycles, respectively, at a current density of 100 mAg^{-1}.

The decrease in specific capacitance in the second and third cycles is due to the formation of undecomposable products during the discharge process[36].

As shown in Figure 5-(b), by increasing the ratio of super P/$Ti_3C_2T_x$ to 30:60, the specific capacity of the battery reached up to 1116 $mAhg^{-1}$ in the 1st cycle, and 612 $mAhg^{-1}$ and 308 $mAhg^{-1}$ in the 2nd and 3rd cycles, respectively, at a current density of 100 mAg^{-1}.

By comparing the curves presented in Figure 5, it is observed that by increasing super P to 30%, the specific capacity is increased by up to 180%. This increase can be attributed to the enhanced electrical conductivity of the cathode and de-stacking of the MXene layers.

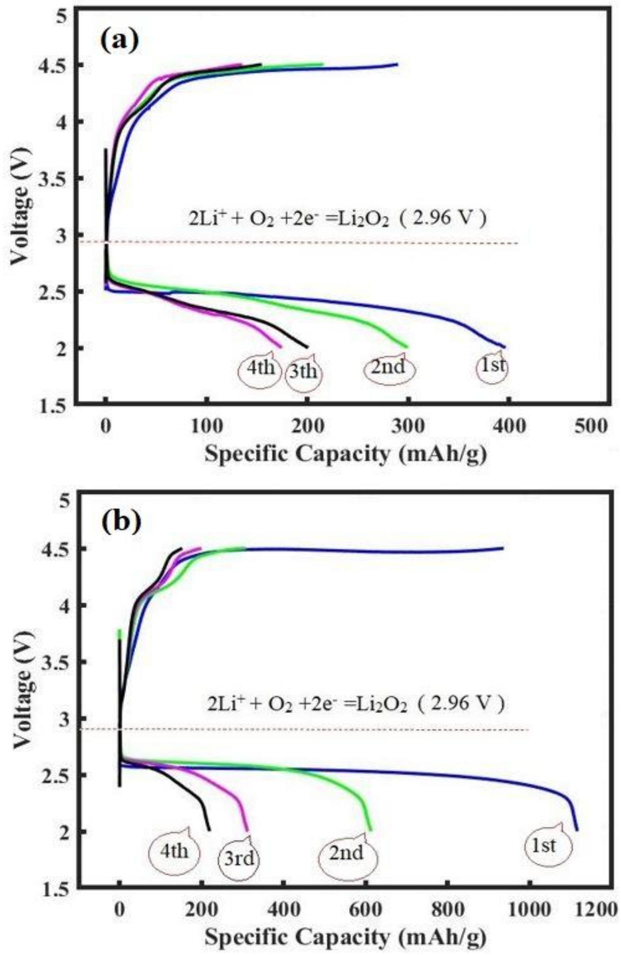

Figure 5. Discharge-charge profiles of super p/$Ti_3C_2T_x$ cathodes at 100 mAg^{-1} with (a) 10% and (b) 30% Super P, respectively.

To further investigate the electrochemical behavior of $Ti_3C_2T_x$ and Super P in Li-Oxygen cathode, these two materials were separately used in Li-Oxygen cells as active materials. The Nyquist curves of these two cells are depicted in Figure 6. These curves have been fitted using the equivalent circuit model (the inset of Figure 6), which includes both double-layer capacitance (CPE1) and pseudo-capacitance (CPE2) (25, 26). Based on this model, R_s (total DC resistance) and R_{ct} (charge transfer resistance) are displayed in Table 1.

[DOI: 10.22068/ase.2024.674]

.
Referring to Table 1, one can see that Super P has a lower R_s but higher R_{ct} than $Ti_3C_2T_x$, which implies the higher electrical conductivity of Super P and higher charge transfer capability of MXene. In addition, due to the lower slope of the Nyquist curve in the MXene-based Li-Oxygen cathode, it can be demonstrated that the faradic mechanism is more probable in this electrode than in the Super P-based electrode.

Table 1. Resistance values for the fabricated electrode were obtained from Nyquist plot fitting using an equivalent circuit

Li-Oxygen cathode	R_s (Ω)	R_{ct} (Ω)
Super p	31.5	209
$Ti_3C_2T_x$	41.5	129.5

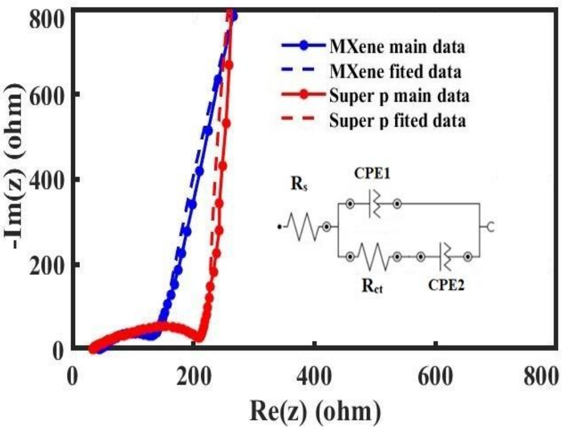

Figure 6. Nyquist curves of $Ti_3C_2T_x$ and Super P/ $Ti_3C_2T_x$ based Li-Oxygen cell before the first discharge cycle.

The cycle life profiles of $Li-O_2$ batteries with Super P/$Ti_3C_2T_x$ cathodes at different percentage of Super P (10% and 30%) are presented in Figure 7. Like most of other reported Li-Oxygen batteries both of the batteries are decayed after several cycles due to variety of reasons such as electrode degradation, limited reaction kinetics, dendrite formation, etc. However, the battery with a higher amount of Super P exhibits better cyclic stability.

To investigate the reaction kinetics, the CV curves of the pure $Ti_3C_2T_x$ and pure Super P based Li-Oxygen cells at a scan rate of 5 mVS^{-1} and a voltage window of 2 to 4.5 V are present in Figures 8(a)&(b). The CV curves of these two cells have almost the same shape with identical peak positions (2.5 V for the ORR and 3.4 V for the OER), indicating that the charge storage mechanism is the same in both electrodes. These peaks are related to the oxygen reduction and evolution reactions implying that charge storage is carried out by the formation and decomposition of Li_2O_2 species. It is worth mentioning that the OER peak at 2.5 V is in good agreement with plateau of the discharge profiles in Figure 5.

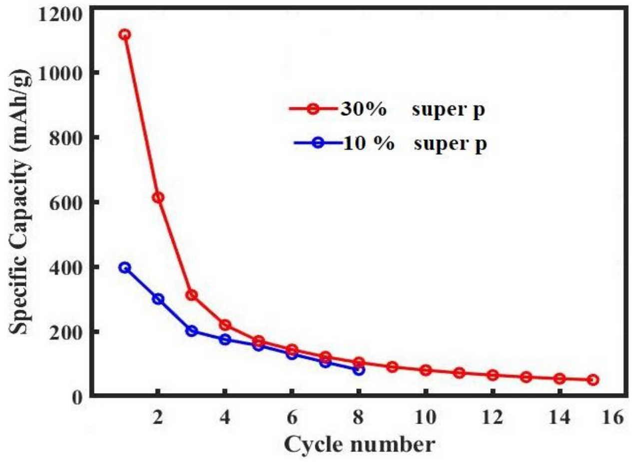

Figure 7. Specific capacity profile of $Li-O_2$ battery with super p/$Ti_3C_2T_x$ cathodes at 100 mAg^{-1} with 10% and 30% super p to cycle number.

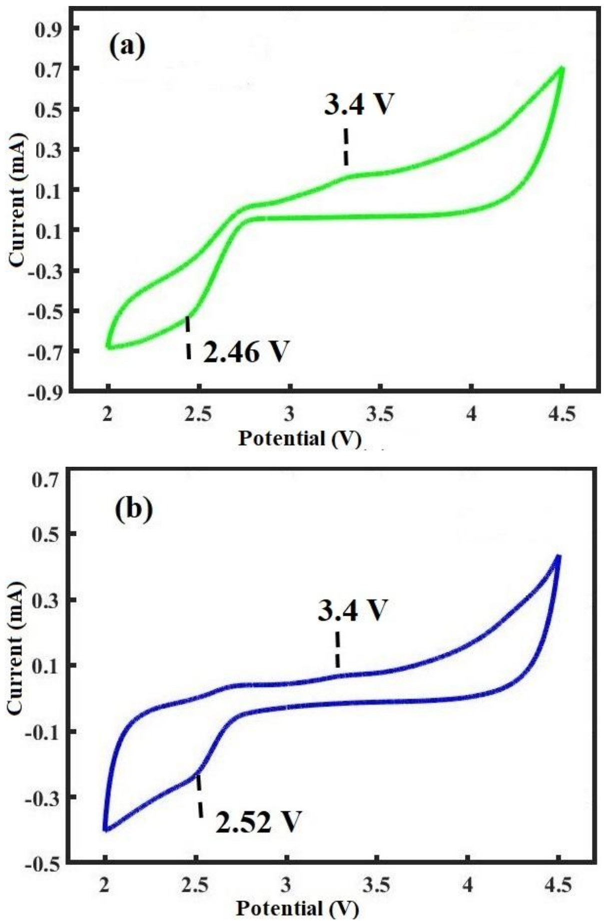

Figure8. CV curves of $Li-O_2$ batteries with (a) $Ti_3C_2T_x$, and (b) super p nanocomposite at a sweep rate of 5 mV s^{-1}.

onsidering our results, it seems that increasing the amount of Super P as a conductive material in the MXene-based Li-O_2 battery enhances electrochemical performance, including specific capacity and electrochemical stability. While MXene layers are known to be highly conductive 2D materials, the improvement in performance cannot be attributed solely to the high conductivity of Super P, although it does have a positive effect. A precise comparison of the SEM images of pristine $Ti_3C_2T_x$ and Super P/ $Ti_3C_2T_x$ in Figure 2 shows that the Super P nanoparticles are distributed between the MXene nanosheets, increasing the distance between the nanostacks and nanosheets.

This configuration can facilitate the diffusion of Li ions and oxygen and their easier penetration and exit from the MXene layers, which, in turn, leads to a higher capability for Li_2O_2 formation and decomposition.

In addition, both $Ti_3C_2T_x$ and Super P have been reported to have a catalytic effect on the formation and decomposition of Li_2O_2. It can be speculated that the combination of these two materials has a synergistic effect that improves electrochemical performance.

Referring to our results and other studies, we speculate that it is valuable to investigate the combination of MXene and Super P in depth to determine the suitable amount of each material in the composite and to find an effective method for distributing the Super P grains between the MXene nanolayers. This approach aims to enhance the electrochemical performance of the Li-O_2 cathode by utilizing the synergistic effects of Super P and $Ti_3C_2T_x$ layers.

4. Conclusion

This work investigated the effect of super p on the discharge-specific capacity of $Ti_3C_2T_x$-based Li-O_2 battery cathode. It was observed that the discharge-specific capacity was improved up to 180% by increasing the ratio of super P solely around 20%.

References

[1] Kwak, W.-J., et al., Lithium–oxygen batteries and related systems: potential, status, and future. Chemical Reviews, 2020. **120**(14): p. 6626-6683.

[2] Imanishi, N., A.C. Luntz, and P. Bruce, The lithium air battery: fundamentals. 2014: Springer.

[3] Zheng, X., et al., In situ decoration of CoP/$Ti_3C_2T_x$ composite as efficient electrocatalyst for Li-oxygen battery. Chinese Chemical Letters, 2023. **34**(1): p. 107152.

[4] Kannan, K., et al., Current trends in MXene-based nanomaterials for energy storage and conversion system: a mini review. Catalysts, 2020. **10**(5): p. 495.

[5] Zheng, X., et al., Status and Prospects of MXene-Based Lithium–Oxygen Batteries: Theoretical Prediction and Experimental Modulation. Advanced Energy Materials, 2023: p. 2204019.

[6] Yu, H., et al., Surface modified MXene-based nanocomposites for electrochemical energy conversion and storage. Small, 2019. **15**(25): p. 1901503.

[7] Li, X., et al., Nickel oxide nanoparticles decorated highly conductive Ti_3C_2 MXene as cathode catalyst for rechargeable Li–O_2 battery. Journal of Alloys and Compounds, 2020. **824**: p. 153803.

[8] Xia, Q., et al., Recent advances in heterostructured cathodic electrocatalysts for non-aqueous Li–O_2 batteries. Chemical Science, 2022. **13**(10): p. 2841-2856.

[9] Girishkumar, G., et al., Lithium− air battery: promise and challenges. The Journal of Physical Chemistry Letters, 2010. **1**(14): p. 2193-2203.

[10] Christensen, J., et al., A critical review of Li/air batteries. Journal of the Electrochemical Society, 2011. **159**(2): p. R1.

[11] Zheng, X., et al., Theoretical Design and Structural Modulation of a Surface-Functionalized $Ti_3C_2T_x$ MXene-Based Heterojunction Electrocatalyst for a Li–Oxygen Battery. ACS nano, 2022. **16**(3): p. 4487-4499.

[12] Asad, S., et al., Recent Advances in Titanium Carbide MXene (Ti_3C2T_x) Cathode Material for Lithium–Air Battery. ACS Applied Energy Materials, 2022. **5**(10): p. 11933-11946.

[13] Lyu, Z., et al., Recent advances in understanding of the mechanism and control of Li_2O_2 formation in aprotic Li–O_2 batteries. Chemical Society Reviews, 2017. **46**(19): p. 6046-6072.

[14] Song, S., et al., Simultaneous regulation of Li-ion intercalation and oxygen termination decoration on $Ti_3C_2T_x$ MXene toward enhanced oxygen electrocatalysis for Li-O_2 batteries. Chemical Engineering Journal, 2023. **451**: p. 138818.

[15] Singh, B., et al., Preclinical safety assessment of red emissive gold

[DOI: 10.22068/ase.2024.674]

nanocluster conjugated crumpled MXene nanosheets: a dynamic duo for image-guided photothermal therapy. Nanoscale, 2023. **15**(6): p. 2932-2947.

[16] Naguib, M., M.W. Barsoum, and Y. Gogotsi, Ten years of progress in the synthesis and development of MXenes. Advanced Materials, 2021. **33**(39): p. 2103393.

[17] Ronnasi, B., et al., α-NSA doped PPy@ $Ti_3C_2T_x$ hybrid material as a high-performance supercapacitor electrode. Journal of Materials Research, 2022. **37**(22): p. 3965-3975.

[18] Azadvari, R., et al., Effect of ultra-sonication, vacuum drying, and carbon coating on the super-capacitive behavior of $Ti_3C_2T_x$ MXene. Journal of Physics D: Applied Physics, 2023. **57**(4): p. 045501.

[19] Lamiel, C., et al., MXene in core–shell structures: research progress and future prospects. Journal of Materials Chemistry A, 2022. **10**(27): p. 14247-14272.

[20] Ahmadian, Z., et al., Stable N-doped $Ti_3C_2T_x$ gas sensors for recoverable detection of ammonia at room temperature. Ceramics International, 2023. **49**(23): p. 38635-38643.

[21] Lipatov, A., et al., Effect of synthesis on quality, electronic properties and environmental stability of individual monolayer Ti_3C_2 MXene flakes. Advanced Electronic Materials, 2016. **2**(12): p. 1600255.

[22] Alhabeb, M., et al., Guidelines for synthesis and processing of two-dimensional titanium carbide ($Ti_3C_2T_x$ MXene). Chemistry of Materials, 2017. **29**(18): p. 7633-7644.

[23] Thakur, A., et al., Step-by-Step Guide for Synthesis and Delamination of $Ti_3C_2T_x$ MXene. Small Methods, 2023: p. 2300030.

[24] Ahmadian, Z., et al., The effect of ball-milling parameters on the structures of Ti_3AlC_2 MAX phase and resultant Ti3C2Tx MXene. Journal of Ultrafine Grained and Nanostructured Materials, 2022. **55**(2): p. 112-121.

[25] Mohammadi, S., et al., High-capacity freestanding supercapacitor electrode based on electrospun $Ti_3C_2T_x$ MXene/PANI/PVDF composite. Heliyon, 2024. **10**(22).

[26] Seredych, M., et al., High-temperature behavior and surface chemistry of carbide MXenes studied by thermal analysis. Chemistry of Materials, 2019. **31**(9): p. 3324-3332.

[27] Nam, S., et al., Bimetal Organic framework–Ti3C2Tx MXene with metalloporphyrin electrocatalyst for lithium–oxygen batteries. Advanced Functional Materials, 2023. **33**(1): p. 2210702.

[28] Zhao, W., et al., Urchin-like NiO–NiCo 2 O 4 heterostructure microsphere catalysts for enhanced rechargeable non-aqueous Li–O_2 batteries. Nanoscale, 2019. **11**(1): p. 50-59.

[29] Dong, Y., et al., Mxene/alginate composites for lead and copper ion removal from aqueous solutions. RSC advances, 2019. **9**(50): p. 29015-29022.

[30] Wang, Y., Y. Zhou, and Y. Wang, Humidity activated ionic-conduction formaldehyde sensing of reduced graphene oxide decorated nitrogen-doped MXene/titanium dioxide composite film. Sensors and Actuators B: Chemical, 2020. **323**: p. 128695.

[31] Lee, E., et al., Room temperature gas sensing of two-dimensional titanium carbide (MXene). ACS applied materials & interfaces, 2017. **9**(42): p. 37184-37190.

[32] VahidMohammadi, A., et al., Thick and freestanding MXene/PANI pseudocapacitive electrodes with ultrahigh specific capacitance. Journal of Materials Chemistry A, 2018. **6**(44): p. 22123-22133.

[33] Du, X., et al., $Ti_3C_2T_x$@ PDA-integrated polyurethane phase change composites with superior solar-thermal conversion efficiency and improved thermal conductivity. ACS Sustainable Chemistry & Engineering, 2020. **8**(14): p. 5799-5806.

[34] Scheibe, B., et al., Study on the magnetic properties of differently functionalized multilayered Ti3C2Tx MXenes and Ti-Al-C carbides. Applied Surface Science, 2019. **479**: p. 216-224.

[35] Haq, Y.-U., et al., Synthesis and characterization of 2D MXene: Device fabrication for humidity sensing. Journal of Science: Advanced Materials and Devices, 2022. **7**(1): p. 100390.

[36] Wang, Y. and L. Hao, Effects of cathode structure on the discharge performance of non-aqueous Li-O_2 batteries. Electrochimica Acta, 2022. **425**: p. 140703.